IOP Publishing Physica Scripta
Phys. Scr. 95 (2020) 035506 (12pp) https://doi.org/10.1088/1402-4896/ab49e8

Investigation of thin-film p-$BaSi_2$/n-CdS heterostructure towards semiconducting silicide based high efficiency solar cell

Md. Mahabub Alam Moon[1], Md. Hasan Ali[1], Md. Ferdous Rahman[1,2], Abdul Kuddus[2], Jaker Hossain[2] and Abu Bakar Md. Ismail[2]

[1] Department of Electrical and Electronic Engineering, Begum Rokeya University, Rangpur; Rangpur 5400, Bangladesh
[2] Solar Energy Laboratory, Department of Electrical and Electronic Engineering, University of Rajshah; Rajshahi 6205, Bangladesh

E-mail: jak_apee@ru.ac.bd

Received 6 June 2019, revised 8 September 2019
Accepted for publication 1 October 2019
Published 3 February 2020

Abstract

In this article, semiconducting Barium Silicide ($BaSi_2$) absorber based Al/SnO_2: F/CdS/$BaSi_2$: B/Cu novel heterostructure thin-film solar cell (TFSC) has been studied in details. The solar cell has been numerically simulated and intensely analyzed by Solar cell Capacitance Simulator (SCAPS). Layer thickness was varied from 100 to 3000 nm for p^+-$BaSi_2$ absorber, 20 to 200 nm for both n-CdS buffer, and n^+-SnO_2:F window layers to optimize the device. Hitherwards, the impurities concentration for acceptor (N_A) and donor (N_D) ions was optimized for each layer through ample variation. The influence of single-donor and acceptor type bulk defect densities has been investigated thoroughly in p^+-$BaSi_2$ and n-CdS materials, respectively. An efficiency >30% is achievable ideally with a 2 μm thick $BaSi_2$ absorber without incorporating defects whereas it reduces to 26.32% with only 1.2 μm thick absorber including certain amount of defects. Cell thermal stability and alteration of cell parameters were studied under cell operating temperature from 273 to 473 °K. Finally, the effect of series (R_s) and shunt (R_{sh}) resistances on proposed cell has been investigated meticulously. This newly designed solar cell structure proclaims the chance of fabricating a resourceful, low cost, and highly efficient TFSC near future.

Keywords: $BaSi_2$ absorber, CdS buffer, optimization, SCAPS simulation, SnO_2:F window, thin-film solar cell

(Some figures may appear in colour only in the online journal)

1. Introduction

To convert sunlight into electrical energy proficiently, resourceful, cost effective, and highly efficient solar cell is a must. At present, world energy society is still looking for new types of solar cell besides Silicon wafer based first generation and thin-film based second generation (2G) solar cells. In this aspect, semiconducting Barium Silicide ($BaSi_2$) based thin-film solar cell (TFSC) can be an optimistic solution.

An alkaline-earth metal, Barium (Ba) having atomic number 56 is a block S, group 2, and period 6 element. Ba metal is soft in its elemental form and silvery-gray in colour [1]. The very popular semiconductor material Silicon (Si) having atomic number 14 is a block P, group 14, and period 3 element. $BaSi_2$ is usually right away available in most volumes: high purity, submicron, and nanopowder forms [1]. Trigonal, cubic, and orthorhombic are the three major crystal configurations of $BaSi_2$.

For use in photovoltaic (PV) applications, the orthorhombic $BaSi_2$ is the most suited type due to its wide band gap energy of 1.1–1.35 eV and high stability at room temperature (RT) and circumambient pressure [2]. Comprising Ba and Si,

the Earth's abundant semiconducting $BaSi_2$ can be utilized to fabricate a promising low cost TFSC. It is a praiseworthy absorber material for TFSC due to its favourable optoelectronic properties such as high optical absorption coefficient (α) reaching 3×10^5 cm^{-1} [3–5], nearly optimum indirect energy band gap, E_g of 1.3 eV [6–10], long minority carrier diffusion length of 10 μm [4, 6, 10, 11], and lifetime of 14 μs [4, 8]. Moreover, its absorption coefficient is 30 [12] to 40 [7] times larger than that of the single crystalline-Silicon (c-Si). For $BaSi_2$ solar cell, photon absorption begins at 1.3 eV and goes to maximum at 1.5 eV. For a 900 nm thick film, this range is even modified to a wider range of 1.3–1.7 eV [13, 14]. The band gap of $BaSi_2$ material can further be tuned up to 1.4 eV to go with the solar spectrum by introducing one of the group 2 element namely Strontium (Sr) impurities [2, 15]. The diffusion length for minority charge carrier of $BaSi_2$ in Silicon (111 plane) is much larger than that in Silicon (001 plane), with values of 8.6 μm and 1.5 μm, respectively [2]. Concerning theoretical and experimental evaluation [2–4, 6–10, 12–17], $BaSi_2$ is referred to as a suitable absorber material for TFSCs.

In some experimental works, 9% [18] and 9.9% [19] efficiencies were confirmed by p-$BaSi_2$ on Si (111 plane) and $BaSi_2$/c-Si heterojunction solar cell configurations, respectively, both made by MBE method. Theoretically an efficiency of 22.5% has been achieved by n^+-$BaSi_2$/p-$BaSi_2$ and p^+-$BaSi_2$/n-$BaSi_2$ homojunction solar cells with 5×10^{19} cm^{-3} dopants in 2 μm thick absorber material [6]. Under perfect conditions, cell power conversion efficiency (PCE) of ~25% is expected for a 2 μm thick $BaSi_2$ homojunction solar cell [20]. In another simulation, the double-junction perovskite/$BaSi_2$ tandem structure with <2 μm thickness offers conversion efficiency up to 28% [21]. By solving the equations of charge transport with optical generations, 30.4% efficiency at cell level was reported in [22] by a 2.3 μm thick n-Si/i-$BaSi_2$/p-Si TFSC taking $BaSi_2$ energy band gap of 1.086 eV. By another numerical simulation of optimized $BaSi_2$/metal based 2 μm thick Schottky-junction solar cell, highest efficiencies of ~24.12% ($N_D = 10^{15}$ cm^{-3}) and 25.28% ($N_D = 10^{18}$ cm^{-3}) were achieved [23].

For ease of large scale high deposition rate with lower cost, to grow polycrystalline $BaSi_2$ films on Si or glass substrate, Radio Frequency magnetron sputtering technique was adopted [6]. On Si (111 plane) and EAGLE XG glass substrate, single-phase $BaSi_2$ film can be grown at a high temperature of 500 °C and 600 °C [4]. The $BaSi_2$ film can also be grown on Si or quartz substrate by molecular beam epitaxy (MBE) [10, 11, 14, 15, 17, 18] and vacuum evaporation [4, 24] methods.

In this present work, we make use of Cadmium Sulphide (CdS) to act as the n-type heterojunction partner in p-type $BaSi_2$ solar cell. Now-a-days CdS is boastfully used as a common n-type partner in CIGS, and CdTe TFSCs [25–28]. We use Fluorine doped Tin Oxide, FTO (SnO_2:F) as the window layer. We recommend Soda Lime Glass (SLG) for being the substrate for low cost deposition with easy integration. When Si is used as the thick wafer or substrate, it works as an absorber along with the $BaSi_2$ absorber [6]. But,

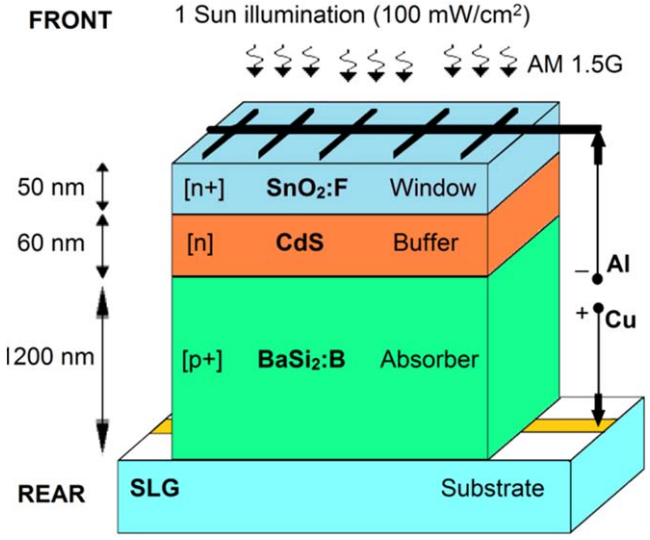

Figure 1. Proposed structure of $BaSi_2$/CdS Thin-film solar cell.

in our designed solar cell structure, SLG glass is used as a substrate for the $BaSi_2$ absorber layer as it does not contribute to light absorption at all. Numerical simulations have been carried out by Solar cell Capacitance Simulator (SCAPS) [29] to analyze the effect of thickness, impurity doping and bulk defect densities, temperature and resistances on device PV performances. Our proposed cell offers higher efficiency (26.32%) than [6, 7, 18–20, 23] with greater open-circuit voltage, V_{oc} (1065 mV) than [6, 7, 17–19, 22, 23]. In addition, obtained fill factor, FF (72.14%) is higher than [7, 18, 19] but lower than [6, 22, 23] whereas, the short-circuit current density, J_{sc} (34.23 mA cm^{-2}) is better than [6, 17, 18, 22, 23].

2. Device modelling and simulation

The simulated thin-film structure of Al/SnO_2: F/CdS/$BaSi_2$: B/Cu is illustrated in figure 1. Boron doped Barium Silicide ($BaSi_2$:B) is utilized here as the p-type active absorber material for TFSC, where CdS acts as a thin n-type buffer layer and SnO_2:F is the highly transparent and conductive oxide (TCO) n^+-type window layer.

Entire simulations and analysis has been carried out by SCAPS (Version: 3.3.07) [29] to measure solar cell output parameters like the conversion efficiency (η), short-circuit current density (J_{sc}), open-circuit voltage (V_{oc}), and fill factor (FF), current at maximum power point (J_{mpp}), voltage at maximum power point (V_{mpp}), carrier current densities, quantum efficiency etc. SCAPS is an opto-electrical simulation tool for one-dimensional (1D) structure of semiconductors up to seven layers. It is a Windows-oriented program developed at the department of Electronics and Information Systems (ELIS) of the University of Gent, Belgium. The program was originally developed for CIGS and CdTe based solar cells. It has also been tested and used for a variety of other types of solar cell.

A one sun (100 mW cm^{-2}) illumination with the global air mass, AM 1.5 G spectrum has been used as the

Table 1. Overview of simulation input data for material properties at $T = 300$ K.

Property	Absorber ($BaSi_2$:B)	Buffer (CdS)	Window (SnO_2:F)
Thickness, W (nm)	1200[a]	60[a]	50[a]
Bandgap, E_g (eV)	1.3 [2, 6–10, 30]	2.4 [29]	3.6 [29]
Electron affinity, χ (eV)	3.3 [2]	4.2 [29]	4 [29]
Dielectric permittivity, ε (relative)	11.17 [22]	10 [29]	9 [29]
CB effective density of states, N_C (cm^{-3})	2.6×10^{19} [2, 6, 20, 23]	2.2×10^{18} [29]	2.2×10^{18} [29]
VB effective density of states, N_V (cm^{-3})	2×10^{19} [2, 6, 20, 23]	1.8×10^{19} [29]	1.8×10^{19} [29]
Electron thermal velocity, S_n ($cm\ s^{-1}$)	1×10^7	1×10^7	1×10^7
Hole thermal velocity, S_p ($cm\ s^{-1}$)	1×10^7	1×10^7	1×10^7
Electron mobility, μ_n ($cm^2\ V^{-1}\ s^{-1}$)	820 [2, 12]	100 [29]	100 [29]
Hole mobility, μ_p ($cm^2\ V^{-1} s^{-1}$)	100 [2]	25 [29]	25 [29]
Shallow uniform donor density, N_D (cm^{-3})	0	1×10^{17}[a]	1×10^{18}[a]
Shallow uniform acceptor density, N_A (cm^{-3})	1×10^{19}[a]	0	0
Defect type	Single donor	Single acceptor	—
Energetic distribution	Uniform	Uniform	—
Bulk defect density, $N(t)$ total (cm^{-3})	1×10^{14}[a]	1×10^{14}[a]	—
Bulk defect density, $N(t)$ peak ($eV^{-1}\ cm^{-3}$)	1×10^{16}[a]	1×10^{16}[a]	—

N.B: [a] is a variable field.

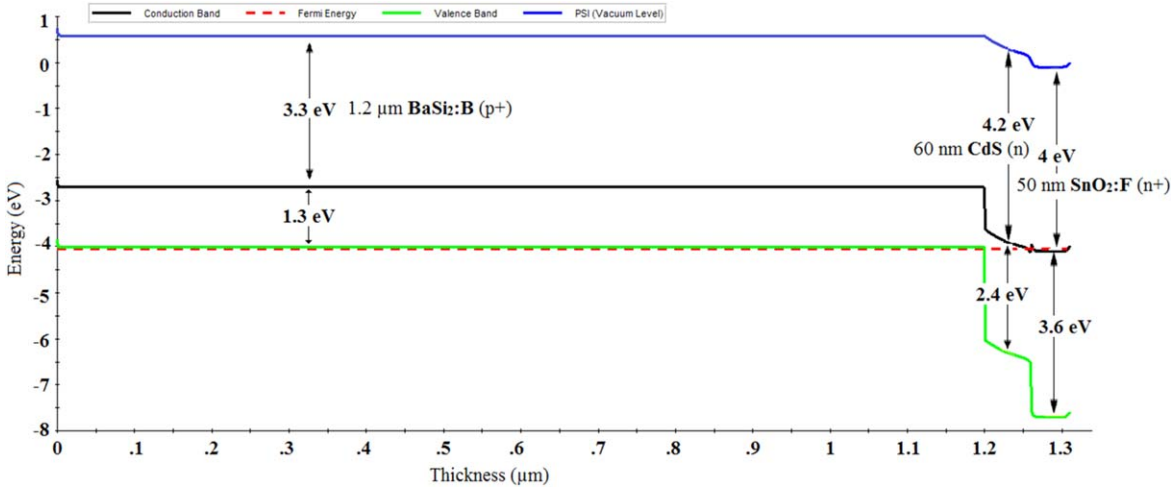

Figure 2. Energy band diagram of p^+-$BaSi_2$:B/n-CdS/n^+-SnO_2:F solar cell in thermodynamic equilibrium.

illumination spectrum. Values for absorption coefficients (α) in cm^{-1} with respect to wavelength (λ) in nm were assigned for $BaSi_2$ from [21], those for CdS, and SnO_2:F from SCAPS [29]. Values for all other required parameters for different layers are employed according to literatures as listed in table 1.

Aluminium (Al) at (110) plane with surface work function, WF of 4.06 eV [31] and Copper (Cu) at (111) plane with WF of 4.94 eV [31] were utilized for the front and rear metallic contacts, respectively. The surface recombination velocity for holes and electrons at front and rear metallic contacts was set to 10^7 $cm\ s^{-1}$.

3. Results and discussion

This study was carried out by numerical analysis to investigate $BaSi_2$ absorber based TFSC that can confirm higher sunlight to electricity conversion efficiency as well as thermal stability with minimal absorber material. Total device depth, doping concentration need to be optimized in thin-film technology to manufacture ultra-thin films with a view to reducing manufacturing time and expenditure, thus to lift up the production throughput.

The thermodynamic equilibrium band diagram of p^+-$BaSi_2$:B/n-CdS/n^+-SnO_2:F heterostructure solar cell is shown schematically in figure 2, illustrated using AMPS-1D simulator [32]. The energy in eV which is required to remove an electron (e^-) from the bottom of conduction band (E_C) to the vacuum level is the electron affinity (χ). Values for χ are 3.3, 4.2, and 4 eV for $BaSi_2$, CdS, and FTO respectively as shown in figure 2. Besides, the corresponding difference between E_C and top of valence band (E_V) i.e. band gap (E_g) is demonstrated for each layer. The Fermi energy level (E_F) position with respect to E_C, and E_V depends on parameters like temperature, doping density, number of free electrons, and holes, and their effective masses. In doped semiconductors, for maintaining the mass action law and to meet

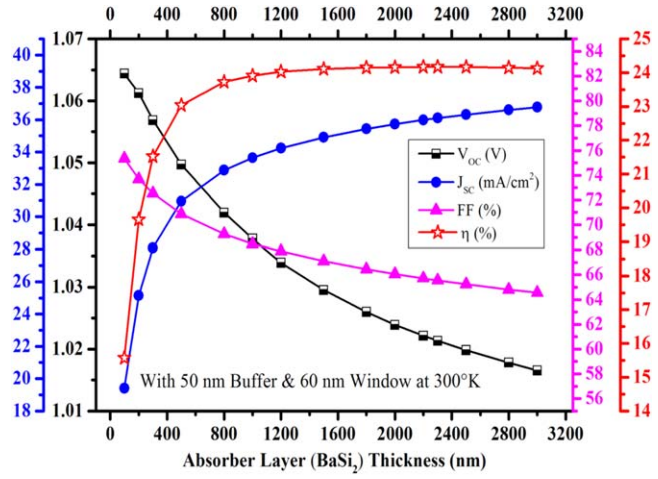

Figure 3. Cell performances w.r.t. absorber layer thickness.

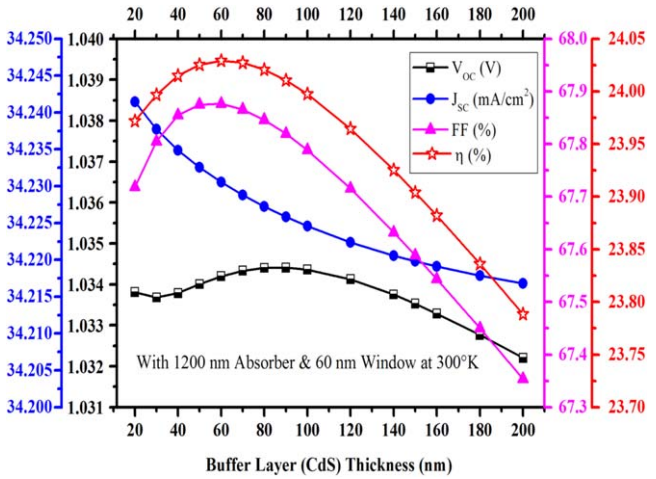

Figure 4. Cell performances w.r.t. buffer layer thickness.

overall charge neutrality or the neutrality equation, E_F moves away from the midgap position either towards E_C in n-type or E_V in p-type semiconductor. For heavily doped degenerate semiconductor materials as in our case, E_F enters the conduction band part in the n^+-FTO layer ($N_D = 5 \times 10^{18}$ cm^{-3}), making FTO metal like. The same occurs with heavily doped p^+-$BaSi_2$ layer ($N_A = 5 \times 10^{19}$ cm^{-3}) such that E_F lies in the valence band itself as pictured in figure 2.

3.1. Effect of $BaSi_2$ absorber layer thickness on PV performances

Taking 50 nm CdS buffer ($N_D = 10^{17}$ cm^{-3}, Defect: 10^{14} cm^{-3}), and 60 nm window ($N_D = 10^{18}$ cm^{-3}), $BaSi_2$ absorber ($N_A = 10^{19}$ cm^{-3}, Defect: 10^{14} cm^{-3}) layer thickness was varied from 100 to 3000 nm at 300 °K. Figure 3 illustrates the deviation of open-circuit voltage (V_{oc}), short-circuit current density (J_{sc}), fill factor (FF), and conversion efficiency (η) with increasing absorber depth.

It is obvious from figure 3 that V_{oc} decreases very slowly from 1.064 to 1.016 V for the entire variation range from 100 to 3000 nm (3 μm). The J_{sc}increases steadily by increasing in absorber layer thicknesses. J_{sc} increases rapidly from 19.412 mA cm^{-2} to 34.232 mA cm^{-2} till 1200 nm and then leads to a gradual increment. With increased absorber layer thickness, recombination is not increased in such a way that it can diminish the J_{sc}. Hence, it increases. But, we must mention that after 1200 nm thickness, it increases very slowly. For instance, J_{sc} increased to 36.77 mA cm^{-2} at 3 μm absorber (only ~2.5 mA increment by the additional 1800 nm absorber). Another reason behind this phenomenon is the long minority carrier diffusion length of 10 μm and lifetime of 14 μs [4] of the $BaSi_2$ absorber layer.

The FF decreases according to the change in V_{oc}, V_{mpp}, J_{sc}, J_{mpp}, and increased series resistance. Cell efficiency, η increases sharply from 15.569% to 24.025% till 1200 nm, then become almost stable or a slight increment till 3000 nm. Lower values for photovoltaic output parameters at lower thickness nearly 600 nm occurs because of the lower absorption probability of photons and high recombination rate of photo-generated charge carriers that recombine before reaching the p-absorber/n-buffer interface. A thicker absorber will easily absorb more photons and their energies, thus to create more electron–hole pairs (EHPs) which significantly increases the photo-generated current. But thicker absorber will cause higher cost accordingly. Hence considering overall consequences, 1200 nm thick absorber layer has been opted to further investigate the model in a systematic manner.

3.2. Effect of CdS buffer layer thickness on PV performances

With 1200 nm thick $BaSi_2$ absorber ($N_A = 10^{19}$ cm^{-3}, Defect: 10^{14} cm^{-3}), and 60 nm thick SnO_2:F window ($N_D = 10^{18}$ cm^{-3}), CdS buffer ($N_D = 10^{17}$ cm^{-3}, Defect: 10^{14} cm^{-3}) layer thickness was varied from 20 to 200 nm at 300 °K. Figure 4 demonstrates the alteration of V_{oc}, J_{sc}, FF, and η with increasing buffer layer thickness.

From numerical simulation outcomes, we find that V_{oc} increases till 90 nm, then decreases but V_{mpp} increases till 60 nm, then decreases. J_{sc} decreases very slowly as if it can be neglected. J_{mpp} increases till 80 nm, then decreases. FF increases till 60 nm, then decreases. η increases till 60 nm, then decreases. With increasing thickness of the buffer, less amount of photons reach the absorber and it causes less EHP generation. Hence the current decreases. However, the decrement happens in such a way that it remains almost constant at 34.2 mA cm^{-2}.

Bearing in mind overall performances in favour of buffer layer, 60 nm thick CdS layer has been chosen to go on with the simulation.

3.3. Cell optoelectrical parameters as a function of absorber layer's acceptor density

With 1200 nm thick $BaSi_2$ absorber (Defect: 10^{14} cm^{-3}), 60 nm thick CdS buffer ($N_D = 10^{17}$ cm^{-3}, Defect: 10^{14} cm^{-3}), and 60 nm thick window ($N_D = 10^{18}$ cm^{-3}), acceptor impurities concentration in absorber layer, N_A was varied from 10^{17} cm^{-3} to 5×10^{20} cm^{-3} at 300 °K.

Group 3 doping materials are generally p-type dopants. The p-type $BaSi_2$ can be realized through various group 3

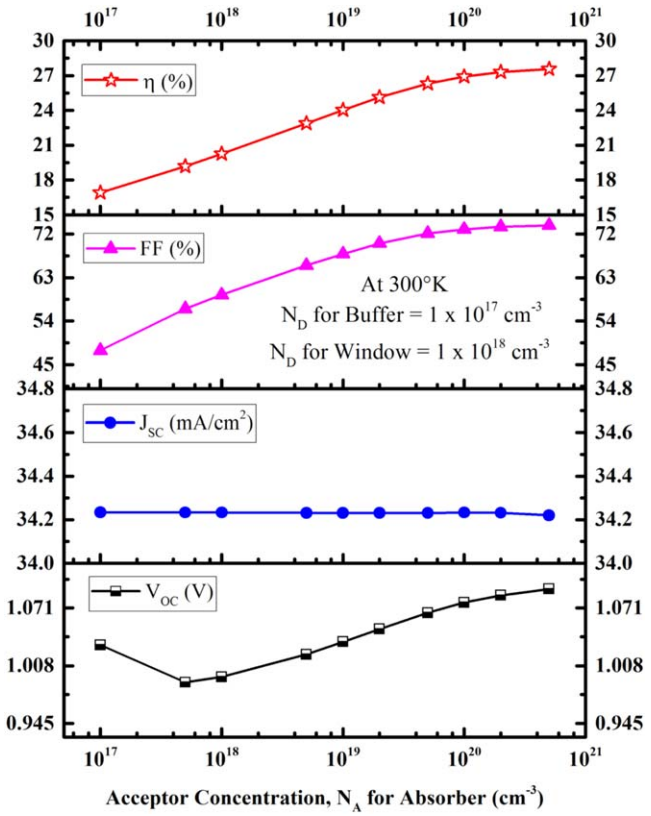

Figure 5. PV performances w.r.t. acceptor impurities in absorber.

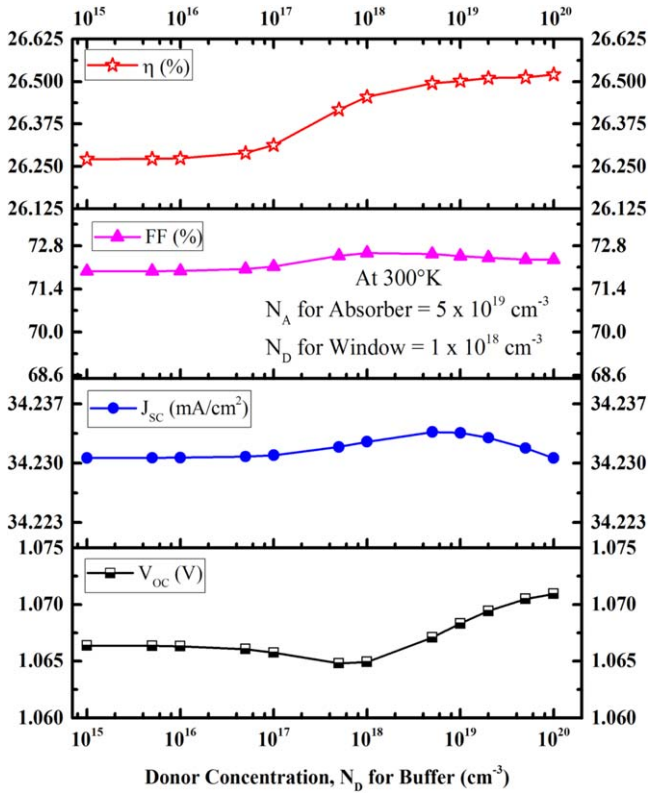

Figure 6. PV performances w.r.t. donor impurities in buffer.

elements like Boron (B), Aluminium (Al), Silver (Ag), Potassium (K), Caesium (Cs), and Indium (In) etc [2, 12]. One exceptional case has been found for Gallium (Ga) which is a group 3 dopant, but constitutes an *n*-type $BaSi_2$ instead of a *p*-type $BaSi_2$ [2]. Among them, Boron dopant can be introduced up to 10^{20} cm^{-3} at RT [12] and it is the only acceptor impurity for obtaining high deposition rate due to low activation energy of Boron in $BaSi_2$ [2]. But the influence of intentionally employed impurities depends stalwartly upon the undoped $BaSi_2$ semiconductor's class. So, we suggest Boron as acceptor type dopant for $BaSi_2$ absorber for our proposed solar cell.

Figure 5 reflects the effects of N_A on cell output parameters. With increasing $BaSi_2$ acceptor concentration (N_A), V_{oc}, and V_{mpp} increase. Voltages at open-circuit and maximum power point (V_{oc} and V_{mpp}) increase with increasing N_A. V_{oc} dropped to 0.989 V at 5×10^{17} cm^{-3} from 1.03 V at 10^{17} cm^{-3} in figure 5. This is due to the higher recombination at that doping level in the high photo-generated voltage region from 0.78 to 1.030 V of the device, compared to the doping at either 10^{17} cm^{-3} or 10^{18} cm^{-3}. Then, V_{oc}increases from 5×10^{17} cm^{-3} till the highest doping of 5×10^{20} cm^{-3}. Also, V_{oc} of 1.030 V at $10^{17}cm^{-3}$ was an extrapolated output given by the simulator. However, the values for V_{mpp} were increased according to the increase in N_A.

J_{sc} decreases very slowly as if negligible. As a result *FF* and η increase. Acceptor ions improve the conductivity in *p*-$BaSi_2$ absorber by introducing a large number of holes. Hole mobility and lifetime for *p*-$BaSi_2$ absorber decrease with increasing acceptor impurity concentration. As a result, diffusion length is reduced. In practice, it is still greater than the active part of the absorber thickness. Therefore, photo-generated current slightly decreases as shown in figure 5. From figure 5, it is evident that cell efficiency increases linearly from less than 17% to higher than 26% till an acceptor concentration of 5×10^{19} cm^{-3}. Then a gradual increase is seen.

With increasing dopant concentration either acceptor or donor, reverse-saturation current reduces, resulting in an increase in V_{oc}. Finally *FF* and η increase.

N_A of the absorber layer was chosen 5×10^{19} cm^{-3} instead of 10^{20} cm^{-3} which is two times of the chosen density. Two times doping does not improve the outputs significantly (it will increase V_{oc} by only 11 mV). On the other hand, high doping in the absorber layer will introduce higher impurity states which will affect the PV performance of the practical devices. High doping concentration requires more growth time with more expense. Hence considering overall performance, 5×10^{19} cm^{-3} N_A for $BaSi_2$ layer has been chosen to continue the investigation.

3.4. Cell optoelectrical parameters as a function of buffer layer's donor density

With 1200 nm thick $BaSi_2$ absorber ($N_A = 5 \times 10^{19}$ cm^{-3}, Defect: 10^{14} cm^{-3}), 60 nm thick CdS buffer (Defect: 10^{14} cm^{-3}), and 60 nm thick window ($N_D = 10^{18}$ cm^{-3}), donor impurities concentration in buffer layer, N_D was varied from 10^{15} cm^{-3} to 10^{20} cm^{-3} at 300 °K.

With increasing CdS donor concentration (N_D) as shown in figure 6, V_{oc} decreases first till 5×10^{17} cm^{-3}, then

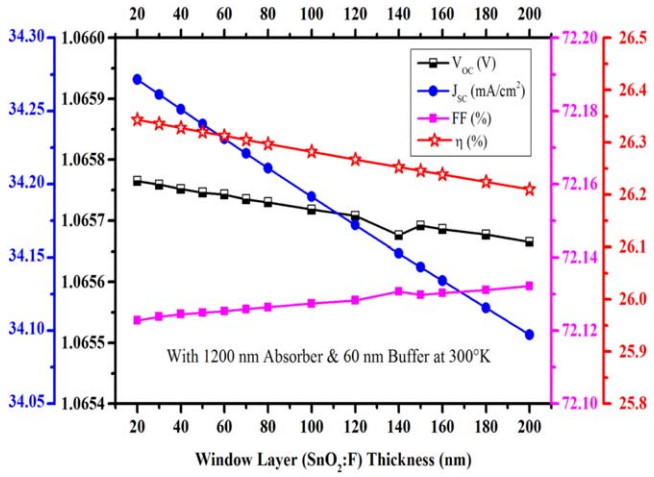

Figure 7. Cell performances w.r.t. window layer thickness.

increases. V_{mpp} decreases till 5×10^{16} cm^{-3}, then increases. J_{sc} increases very slowly till 5×10^{18} cm^{-3}, then decreases. But it can be said to be constant at 34.23 mA cm^{-2}. J_{sc} is almost constant at 31.6 mA cm^{-2}. *FF* increases very slowly till 1×10^{18} cm^{-3}, then decreases. η increases due to the combined effect. Donor ions advance the conductivity in *n*-CdS buffer by adding a large number of free electrons. Thus electron current increases in the cell, resulting better performance.

Believing in a fast and low cost deposition, N_D of 10^{17} cm^{-3} for CdS layer has been optimized to carry out the simulation.

3.5. Effect of SnO_2:F window layer thickness on PV performances

In the cell structure, a transparent and conductive oxide (TCO) namely Fluorine doped Tin Oxide (FTO or SnO_2:F) is used as the window layer. TCO must be highly conductive and should cause a little loss by light absorption. FTO holds lower sheet resistance with more than seven times higher figure of merit compared to Antimony doped Tin Oxide (ATO or SnO_2:Sb) [33]. With 1200 nm thick $BaSi_2$ absorber ($N_A = 5 \times 10^{19}$ cm^{-3}, Defect: 10^{14} cm^{-3}), and 60 nm thick CdS buffer ($N_D = 10^{17}$ cm^{-3}, Defect: 10^{14} cm^{-3}), the window ($N_D = 10^{18}$ cm^{-3}) layer thickness was varied from 20 to 200 nm at 300 °K.

With increasing TCO layer thickness, V_{oc} decreases till 200 nm. From figure 7, it can be said to be constant at 1.065 V. V_{mpp} remains constant at 0.83 V over entire thickness variation. J_{sc} decreases insignificantly. J_{mpp} decreases and *FF* increases till 200 nm. *FF* is said to be constant at 72.1%. Efficiency, η decreases till 200 nm. Photo-generated current decreases as the thicker TCO layer acts as a light trapping material in the structure. Eventually V_{oc} and η decrease.

The PV parameters were changing similarly for the thickness of less than 20 nm. In fact, we have checked these parameters for window thicknesses to the least value of 5 nm. Material's intrinsic properties, sheet resistance and figure of merit of the TCO layer are independent of film thickness [33].

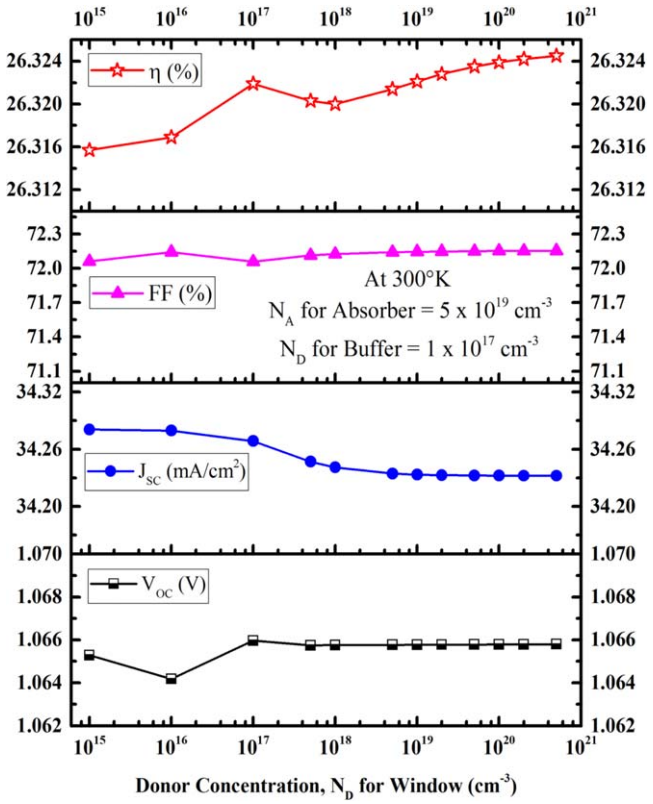

Figure 8. Cell performances w.r.t. donor impurities in window.

However, with increasing TCO layer thickness, all PV parameters decrease since thicker TCO layer causes less light transmission to the absorber layer through it. Also, the resistivity increases rapidly as film thickness decreases from 50 to 10 nm due the discrete and island like structure of the films [34]. Therefore, a trade-off between thickness and PV performance must be made for the optimized output.

As with the increasing TCO layer thickness, V_{oc}, J_{sc}, η decrease; we ought to take a thin TCO layer. In view of fabrication complexity and short-circuit effect, 50 nm thick TCO layer has been opted to further proceed the simulation study because the PV parameters are almost same ($J_{sc} = 34$ mA cm^{-2}, $V_{oc} = 1.065$ V, $FF = 72.1\%$, $\eta = 26\%$) for the FTO thicknesses 20–200 nm.

3.6. Cell optoelectrical parameters as a function of window layer's donor density

With 1200 nm thick $BaSi_2$ absorber ($N_A = 5 \times 10^{19}$ cm^{-3}, Defect: 10^{14} cm^{-3}), 60 nm thick CdS buffer ($N_D = 10^{17}$ cm^{-3}, Defect: 10^{14} cm^{-3}), and 50 nm thick FTO window ($N_D = 10^{18}$ cm^{-3}), donor impurities concentration in window layer, N_D was varied from 10^{15} cm^{-3} to 5×10^{20} cm^{-3} at 300 °K as pictured in figure 8.

With increasing window (TCO) layer donor concentration (N_D), V_{oc} and V_{mpp} increase. V_{oc}halts at 1.065 V. J_{sc} is almost constant. J_{mpp} decreases till 2×10^{19} cm^{-3}, then increases. It can also be said to be constant at 31.69 mA cm^{-2} from 5×10^{18} cm^{-3} to 5×10^{20} cm^{-3}. *FF* increases very slowly from 5×10^{17} cm^{-3} to 5×10^{20} cm^{-3}. η starts

Table 2. PV outputs at 300 °K for cell with different window layers.

Parameter	FTO	AZO
V_{oc} (V)	1.0657	1.0654
J_{sc} (mA cm^{-2})	34.2345	33.9921
FF (%)	72.1414	72.1490
η (%)	26.3214	26.1312
V_{mpp}(V)	0.8304	0.8303
J_{mpp}(mA cm^{-2})	31.6959	31.4718

increasing from 10^{18} cm^{-3} bit by bit. Parameters randomly fluctuate till 10^{17} cm^{-3} as CdS has N_D of 10^{17} cm^{-3} and works as n^+ layer compared to the window, then they become of same doping at concentration of 10^{17} cm^{-3}. FTO window layer causes less impact on cell compared to the CdS buffer. Hence considering overall performance, N_D of 5×10^{18} cm^{-3} for window layer has been opted.

3.7. Cell performances with different window layers

In this section, we discuss the effect of the device on PV parameters with two distinct window layers: FTO and Aluminum doped Zinc Oxide (AZO). The most used TCO in TFSCs is the FTO which has been used extensively in a-Si:H and CdTe solar cells and modules. FTO is stable under ambient conditions, mechanically durable, chemically static, scratch tolerant, and resistant to high temperatures [35]. Factors that govern TCO behaviour are energy band gap (3.3 eV for AZO, 3.6 eV for FTO), work function (4.1 eV for AZO, 4 eV for FTO), and energy level alignment at the heterojunctions. A higher band gap window will be more transparent for low wavelength photons to be passed to and absorbed by the active absorber layer. In other words, FTO shows good visible transparency due to its wide band gap. The simulated QE (λ) panel of the simulator also proves that. We find that the cell with FTO window layer provides greater QE at low wavelength region (90% QE at 300 nm) of incident light spectrum compared to that (70% QE at 300 nm) with the cell having AZO window layer. Again, with 50 nm window, outputs are summarized in table 2 for both cases.

3.8. Influence of bulk defects on cell performances

Donor-like defects in *p*-$BaSi_2$ absorber material and acceptor-like defects in *n*-CdS buffer material were introduced to significantly study the impact of bulk defects on $BaSi_2$ based solar cell parameters. At 300 °K with 60 nm thick CdS buffer ($N_D = 10^{17}$ cm^{-3}), 1200 nm thick $BaSi_2$ absorber ($N_A = 5 \times 10^{19}$ cm^{-3}), and 50 nm FTO window ($N_D = 5 \times 10^{18}$ cm^{-3}) layer; single acceptor-like bulk defect, and single donor-like bulk defect were varied in the range as exposed in figure 9. Figure 9 reflects that all parameters remain almost constant with lower defect densities of 10^{13} cm^{-3}. With increasing defects, values for cell parameters start dropping. For denser bulk defects over 5×10^{13} cm^{-3}, all parameters got worsen. We find that defects in absorber layer influences more than that in buffer layer. For defects in buffer, *FF* and η decreases more rapidly compared to V_{oc} and J_{sc}. This is

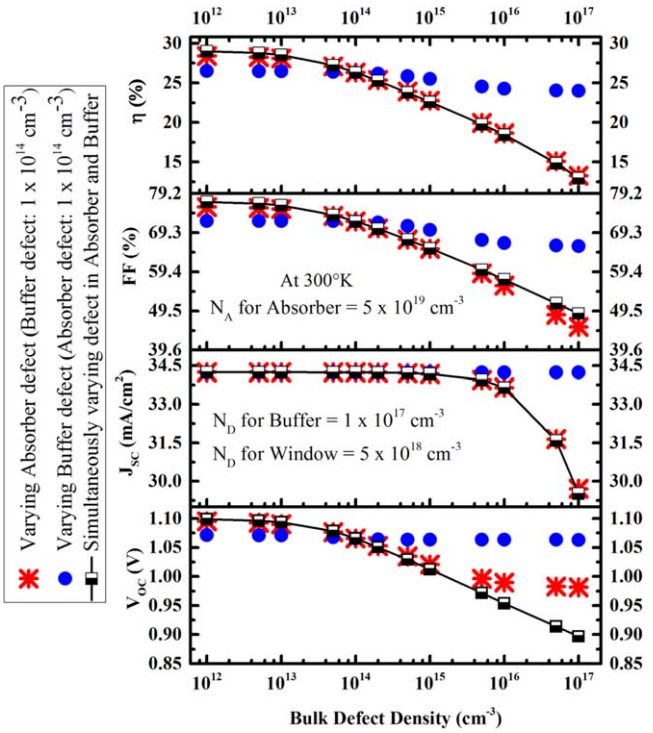

Figure 9. Influence of bulk defect density in absorber and buffer layers.

reasonable because the defect density is then a few orders lower in magnitude than the donor or acceptor concentration. With higher defect density, it becomes easier for the charge carriers to be recombined with opposite charge carriers before reaching the junction. Among the three recombination mechanisms: band-to-band (direct), Auger, and Shockley–Read–Hall (SRH) recombination, mainly the third category is answerable for these dreadful conditions.

Taking $BaSi_2$ absorber ($N_A = 5 \times 10^{19}$ cm^{-3}, Defect: 10^{14} cm^{-3}), 60 nm thick CdS buffer ($N_D = 10^{17}$ cm^{-3}, Defect: 10^{14} cm^{-3}), and 50 nm thick FTO window ($N_D = 5 \times 10^{18}$ cm^{-3}) layer; table 3 summarizes the performance outline for 1.2 and 2 μm thick absorber at 300 °K. It is palpable from table 3 that the cell design with pure materials can exceed 30% efficiency at cell level with a 2 μm thick $BaSi_2$ absorber based single junction solar cell. However, no material can be realized absolutely pure. Our proposed cell offering 26.32% efficiency with only 1.2 μm thick absorber layer can defeat the conventional wafer based c-Si solar cell with utmost efficiency of 26.1% (at ISFH test centre, February 2018) [36].

3.9. Impact of temperature on cell performances

Concerning 1.2 μm thick absorber ($N_A = 5 \times 10^{19}$ cm^{-3}, Defect: 10^{14} cm^{-3}), 60 nm thick buffer ($N_D = 10^{17}$ cm^{-3}, Defect: 10^{14} cm^{-3}), and 50 nm thick window ($N_D = 5 \times 10^{18}$ cm^{-3}) layer, cell operating temperature, *T* was varied over 200 °K from 273 °K to 473 °K. Figure 10 reflects the effects of temperature on cell parameters.

We have determined that the temperature mostly affect the cell at open-circuit voltage (V_{oc}) pessimistically, thus to reduce the cell efficiency. V_{oc}linearly decreases quicker than

Table 3. Performances comparison of modelled cell including and excluding defects at 300 °K.

Cell type	Absorber thickness (μm)	Voltage at open-circuit, V_{oc} (V)	Voltage at maximum power point, V_{mpp} (V)	Current density at short-circuit, J_{sc} (mA cm^{-2})	Current density at maximum power point, J_{mpp} (mA cm^{-2})	Fill Factor, FF (%)	Efficiency, η (%)
With defect	1.2	1.0657	0.8304	34.2345	31.6959	72.1414	26.3214
Without defect	1.2	1.0999	0.9177	34.2406	31.6753	77.1883	29.0709
With defect	2	1.0572	0.8095	35.7313	33.0486	70.8196	26.7545
Without defect	2	1.1011	0.9175	35.7434	33.0634	77.0849	30.3385

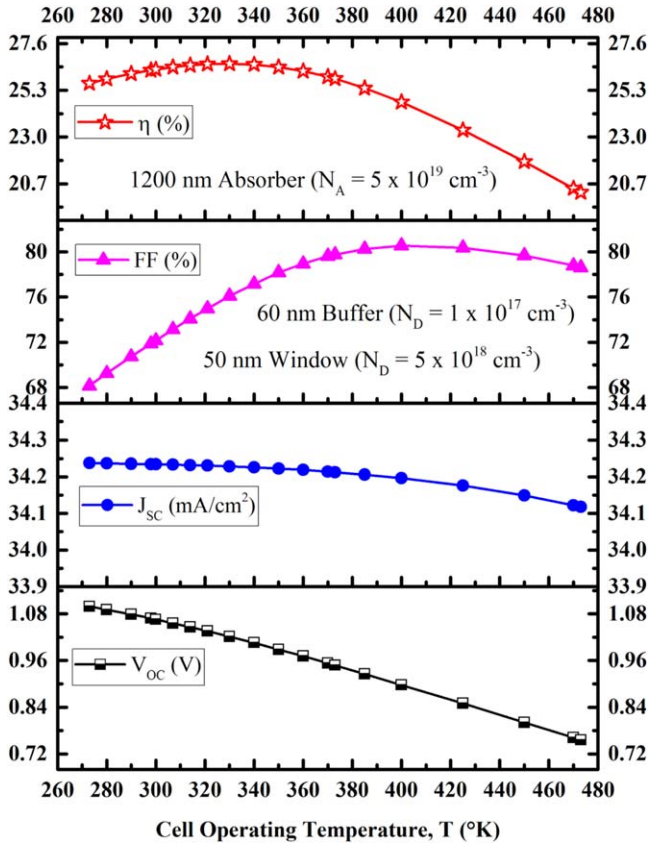

Figure 10. Effect of operating temperature on PV performances.

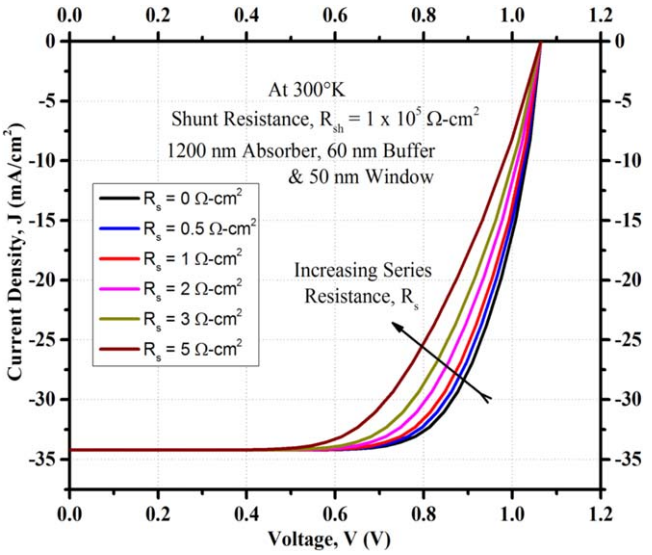

Figure 11. Influence of Series resistance, R_s on *J–V* curve.

J_{sc} as demonstrated by figure 10, consequently a drop off occurs in overall efficiency. More heat in cell increases reverse-saturation current while decreasing the saturation current, ultimately decreases $V_{oc.}$ Semiconductor material's energy band gap (E_g) reduces with increasing temperature. In semiconductor bond model for energy band gap, a fall in the bond energy with increasing temperature reduces E_g [37]. Increased thermal energy causes an increase in electrons energy in that material accordingly. Those highly energized electrons will easily recombine with the holes more often. Thus internal carriers' recombination rate increases resulting in diminishing the $V_{oc}$and η. For high E_g, cell produced voltage is higher and the cell is less dominating by the low temperature. On the contrary, cell is dominated by the high temperature at V_{oc}.

The $J_{sc}$is almost constant at 34.2 mA cm^{-2} for first 100 °K range, then a negligible decrement occurs because of the dominating recombination of a large number of EHPs.

In figure 10, efficiency increases first in the temperature range from 273 °K (25.6394%) to 330 °K (26.6057%), then it starts decreasing till 473 °K. The following discussion may provide the plausible explanation of these phenomena.

The *FF* is the combined effect of the V_{OC}, J_{SC} and those at maximum power point, V_{MPP}, J_{MPP} and can be written as equation (1) [22]

$$FF = \frac{V_{MPP} \times J_{MPP}}{V_{OC} \times J_{SC}}. \quad (1)$$

The PCE, η can be mathematically expressed as equation (2) [22]

$$\eta = \frac{V_{OC} \times I_{SC} \times FF}{P_{in}} \quad (2)$$

where, P_{in} is the incident radiation power (100 mW cm^{-2}) from sunlight. The J_{sc} is almost constant at 34.2 mA cm^{-2} and V_{oc} does not significantly decrease for first 100 °K range compared to the rapid increase in *FF* in this range. *FF* then decreases as shown in figure 10. Depending on these changes, the efficiency increases first in the temperature range from 273 °K to 330 °K. The *FF* increases first till 400 °K since the resistance effect goes down, and after that temperature, it once again decreases due to high electron–hole recombination for thermal runaway and combined effect of V_{oc},V_{mpp}, J_{sc}, and J_{mpp}.

It has been found that in the temperature range of 290 °K to 360 °K, efficiency remains greater than 26% and greatest efficiency of 26.606% at 330 °K. Obtained temperature coefficient of $-0.0268\%/°K$ discloses the possibility of having a nearly thermally constant solar cell for the proposed structure.

3.10. Influence of series and Shunt resistances on the proposed solar cell

At 300 °K with 1200 nm thick $BaSi_2$ absorber ($N_A = 5 \times 10^{19}$ cm^{-3}, Defect: 10^{14} cm^{-3}), 60 nm thick CdS buffer ($N_D = 10^{17}$ cm^{-3}, Defect: 10^{14} cm^{-3}), and 50 nm FTO window ($N_D = 5 \times 10^{18}$ cm^{-3}) layer, series resistance, R_s is varied. In this case, shunt resistance, R_{sh} of 10^5 Ω cm^2 is kept constant. Figures 11 and 12 show corresponding effect on *J–V* characteristic curve and cell output parameters, respectively.

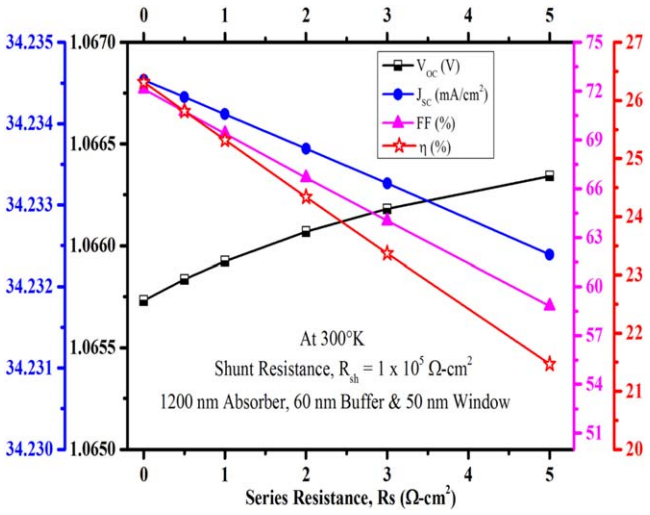

Figure 12. Influence of R_s on cell performances.

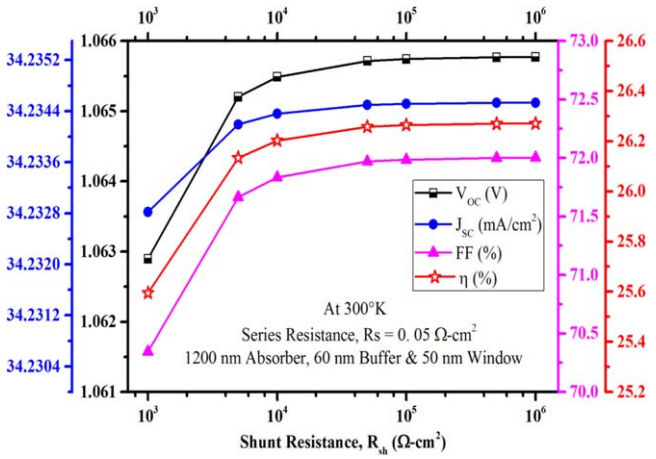

Figure 14. Influence of R_{sh} on cell performances.

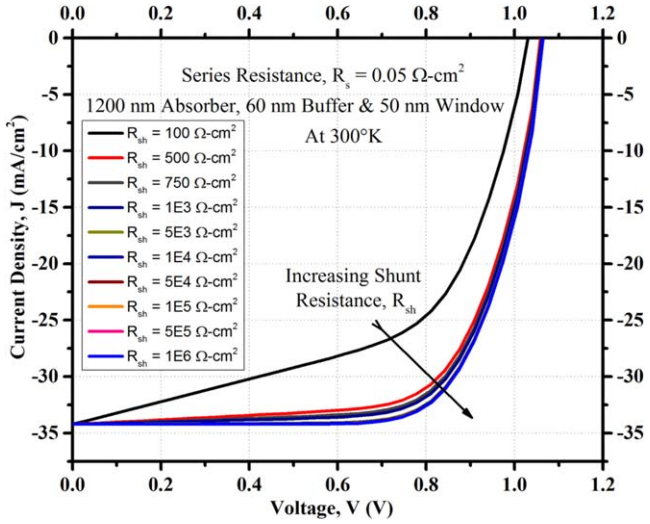

Figure 13. Influence of Shunt resistance, R_{sh} on J–V curve.

In any solar cell, series resistance, R_s is the result of the interface resistance found in the junction of different layers, and also for the front and back metallic contact layers. Series resistance does not affect the solar cell at open-circuit voltage, V_{oc} since overall current through the solar cell, and consequently through the series resistance is zero [37]. It also hampers the short-circuit current, J_{sc} modestly. In fact a negligible increase occurs for V_{oc} as if it can be easily said to be constant at 1.06 V as shown in figure 12. Furthermore J_{sc} decreases faintly with increasing series resistance, but it is also constant at 34.23 mA cm^{-2}. R_s mainly influences the parameters: FF, and η. Figure 11 explores the fact that the J–V curve is extremely influenced by the R_s.

At parameters similar to series resistance depicted above, shunt resistance, R_{sh} is varied. We want to mention that value for R_{sh} was taken 8.84 × 10^5 Ω cm^2 in [21] which is very close to the maximum value of 1 × 10^6 Ω cm^2 of the present work. Here the series resistance, R_s is kept unvarying at 0.05 Ω cm^2 similar to [21]. Figures 13 and 14 explain the corresponding effect of shunt resistance on J–V characteristic curve and cell output parameters, respectively.

When solar cell forms low shunt resistance across the cell, it results a loss in output power. This is due to the existing alternating path for the photo-generated current to flow, offered by that lower shunt resistance. Such an occurrence lessens the quantity of junction current passing through the solar cell junction, thus reducing the cell produced voltage. On the contrary, increasing R_{sh} offers better performances as revealed by figure 14. As illustrated by figure 13, R_{sh} causes a minor effect on solar cell at the short-circuit current density, J_{sc}.

4. Conclusion

In this study, numerical simulations and intensive analysis were performed in a systematic manner to optimize the novel p-$BaSi_2$/n-CdS thin-film heterostructure solar cell. We have investigated thoroughly the influence of absorber, buffer, and window layer thickness, doping impurities concentration, and bulk defect densities on the most important parameters of $BaSi_2$ absorber based solar cell. Lastly, the impact of cell operating temperature as well as series and shunt resistances were studied. To sum up, 1200 nm thick $BaSi_2$:B as the active absorber material with acceptor impurities concentration, N_A of 5 × 10^{19} cm^{-3}, 60 nm thick CdS as the buffer layer with donor impurities concentration, N_D of 10^{17} cm^{-3}, and 50 nm thick SnO_2:F as the window layer with donor impurities concentration, N_D of 5 × 10^{18} cm^{-3} have been opted for the proposed solar cell structure. At AM 1.5 G under 1 Sun illumination (100 mW cm^{-2}) and 300 °K, our proposed Al/SnO_2: F/CdS/$BaSi_2$: B/Cu heterostructure thin-film solar cell allows an efficiency, η of 26.32% (J_{sc} of 34.234 mA cm^{-2}, FF of 72.14%, V_{oc} of 1.065 V, and temperature coefficient of −0.0268%/°K) that certainly indicates the opportunity of fabricating a resourceful, cost effective, and high efficiency thin-film solar cell.

Acknowledgments

The authors would like to appreciate Alex Niemegeers, Marc Burgelman, Stefaan Degrave, Johan Verschraegen, and Koen Decock of the department of ELIS, University of Gent, Belgium for the development of SCAPS simulator and for providing SCAPS software package of the latest version. They would also like to thank Professor Stephen J. Fonash and his team of the Centre for Nanotechnology Education and Utilization of the Pennsylvania State University, USA for supporting them by providing AMPS-1D simulator.

ORCID iDs

Md. Mahabub Alam Moon https://orcid.org/0000-0002-7196-1082
Md. Hasan Ali https://orcid.org/0000-0002-7034-4656
Md. Ferdous Rahman https://orcid.org/0000-0002-0090-2384
Abdul Kuddus https://orcid.org/0000-0001-5204-3844
Jaker Hossain https://orcid.org/0000-0001-7167-8634
Abu Bakar Md. Ismail https://orcid.org/0000-0001-6856-5663

References

[1] Data Sheet: Barium Silicide, American Elements - The Advanced Materials Manufacturer. CAS No. 1304-40-1 https://americanelements.com/barium-silicide-1304-40-1 (Visited on August 2019)
[2] Doorene S 2017 Barium disilicide: development of a novel, low cost and earth abundant absorber material for thin film solar cell applications *MS Thesis* Dept. of Electrical Sustainable Energy, Delft University of Technology, Delft, Netherlands http://resolver.tudelft.nl/uuid:177b86f2-cb70-4e74-b02b-b0ee421c7e36
[3] Pokhrel A, Samad L, Meng F and Jin S 2015 Synthesis and characterization of barium silicide ($BaSi_2$) nanowire arrays for potential solar applications *Nanoscale* **7** 17450–6
[4] Hara K O, Nakagawa Y, Suemasu T and Usami N 2016 Simple vacuum evaporation route to $BaSi_2$ thin films for solar cell applications *Proc. Eng.* **141** 27–31
[5] Toh K, Saito T and Suemasu T 2011 Optical absorption properties of $BaSi_2$ epitaxial films grown on a transparent silicon-on insulator substrate using molecular beam Epitaxy, brief note *Japan. J. Appl. Phys.* **50** 1–2
[6] Deng Q, Chen H, Liao H, Chen L, Wang G, Wang S and Shen Y 2019 Numerical simulation and optimization of $Si/BaSi_2$ heterojunction and $BaSi_2$ homojunction solar cells *J. Phys. D: Appl. Phys.* **52** 1–11
[7] Deng T, Sato T, Xu Z, Takabe R, Yachi S, Yamashita Y, Toko K and Suemasu T 2018 p-$BaSi_2$/n-Si heterojunction solar cells on Si(001) with conversion efficiency approaching 10%: comparison with Si(111), Letter *Appl. Phys. Express* **11** 1–5062301
[8] Kumar M, Umezawa N and Imai M 2014 $BaSi_2$ as a promising low-cost, earth-abundant material with large optical activity for thin-film solar cells: a hybrid density functional study *Appl. Phys. Express* **7** 1–4071203
[9] Nakamura T, Suemasu T, Takakura K, Hasegawa F, Wakahara A and Imai M 2002 Investigation of the energy band structure of orthorhombic $BaSi_2$ by optical and electrical measurements and theoretical calculations *Appl. Phys. Lett.* **81** (6) 1032–4
[10] Takeuchi H, Du W, Baba M, Takabe R, Toko K and Suemasu T 2015 Characterization of defect levels in undoped n-$BaSi_2$ epitaxial films on Si(111) by deep-level transient spectroscopy *Japan. J. Appl. Phys.* **54** 1–507JE01
[11] Tsukahara D, Baba M, Watanabe K, Kimura T, Hara K O, Du W, Usami N, Toko K, Sekiguchi T and Suemasu T 2015 Cross-sectional potential profile across a $BaSi_2$ pn junction by Kelvin probe force microscopy, Rapid Communication *Japan. J. Appl. Phys.* **54** 030306
[12] Khan M A and Suemasu T 2017 Donor and acceptor levels in impurity-doped semiconducting $BaSi_2$ thin films for solar-cell application *Phys. Status Solidi A* **214** 1–10
[13] Fomin D, Dubov V, Galkin K, Galkin N, Batalov R and Shustov V 2017 Formation and properties of crystalline $BaSi_2$ thin films obtained by solid phase epitaxy on Si(111) *JJAP Conf. Proc.* **5** 011203
[14] Matsumoto Y, Tsukada D, Sasaki R, Takeishi M and Suemasu T 2009 Photoresponse properties of semiconducting $BaSi_2$ epitaxial films grown on Si(111) substrates by molecular beam epitaxy *Appl. Phys. Express* **2** 021101
[15] Du W, Saito T, Khan M A, Toko K, Usami N and Suemasu T 2012 Effect of Solid-phase-epitaxy Si layers on suppression of Sb diffusion from Sb-doped n-$BaSi_2$/p-Si tunnel junction to undoped $BaSi_2$ overlayers *Japan. J. Appl. Phys.* **51** 04DP01
[16] Vismara R, Isabella O and Zeman M 2017 Back-contacted $BaSi_2$ solar cells: an optical study *Opt. Express* **25** A402–8
[17] Du W, Takabe R, Baba M, Takeuchi H, Hara K O, Toko K, Usami N and Suemasu T 2015 Formation of $BaSi_2$ heterojunction solar cells using transparent MoO_x hole transport layers *Appl. Phys. Lett.* **106** 122104
[18] Tsukahara D, Yachi S, Takeuchi H, Takabe R, Du W, Baba M, Li Y, Toko K, Usami N and Suemasu T 2016 p-$BaSi_2$/n-Si heterojunction solar cells with conversion efficiency reaching 9.0% *Appl. Phys. Lett.* **108** 152101
[19] Yachi S, Takabe R, Takeuchi H, Toko K and Suemasu T 2016 Effect of amorphous Si capping layer on the hole transport properties of $BaSi_2$ and improved conversion efficiency approaching 10% in p-$BaSi_2$/n-Si solar cells *Appl. Phys. Lett.* **109** 072103
[20] Suemasu T 2015 Exploring the possibility of semiconducting $BaSi_2$ for thin-film solar cell applications *Japan. J. Appl. Phys.* **54** 07JA01
[21] Vismara R, Isabella O and Zeman M 2016 Organometallic halide perovskite/barium di-silicide thin-film double-junction solar cells *Proc. SPIE, Photonics for Solar Energy Systems VI* 9898 *(Brussels, Belgium, April 29, 2016)* 98980J
[22] Huang J, Lee K and Tseng Y 2014 Analysis of the high conversion efficiencies β-$FeSi_2$ and $BaSi_2$ n-i-p thin film solar cells *J. Nanomater.* **2014** 238291
[23] Chen L, Chen H, Deng Q, Wang G and Wang S 2018 Numerical simulation of planar $BaSi_2$ based Schottky junction solar cells toward high efficiency *Solid-State Electron.* **149** 46-51
[24] Nakagawa Y, Hara K O, Suemasu T and Usami N 2016 On the mechanism of $BaSi_2$ thin film formation on Si substrate by vacuum evaporation *Proc. Eng.* **141** 23-26
[25] Moon M M A, Rahman M F and Ismail A B M 2018 Optimization of active region thickness of CdTe/CdS thin film superstrate solar cell to achieve ~25% efficiency: a simulation approach *2018 Int. Conf. on Comp., Commu., Chem., Mater. Electron. Eng. (Rajshahi, Bangladesh, February 8-9, 2018)* (IEEE) (INSPEC Accession No. 18113372) (https://doi.org/10.1109/IC4ME2.2018.8465600)

[26] Ali M H, Moon M M A and Rahman M F 2019 Study of ultra-thin CdTe/CdS heterostructure solar cell purveying open circuit voltage ∼1.2 V *Mater. Res. Express* **6** 095515

[27] Moon M M A, Rahman M F, Hossain J and Ismail A B M 2019 Comparative study of the second generation a-Si:H, CdTe, and CIGS thin-film solar cells *Adv. Mater. Res.* **1154** 102–11

[28] Kuddus A, Rahman M F, Ahmmed S, Hossain J and Ismail A B M 2019 Role of facile synthesized V_2O_5 as hole transport layer for CdS/CdTe heterojunction solar cell: Validation of simulation using experimental data *Superlattices Microstruct.* **132** 1–10106168

[29] Niemegeers A, Burgelman M, Degrave S, Verschraegen J and Decock K 2018 *SCAPS (Version: 3.3.07) Manual* November 7, 2018 (Gent, Belgium: University of Gent) http://scaps.elis.ugent.be/ (Visited on August 2019).

[30] Suemasu T 2015 Possibility of Si-based new material for thin-film solar cell applications *J. Phys.: Conf. Ser.* **596** 012005

[31] Data Sheet: Electron Work Function of the Elements, Physical Chemistry Laboratory, Washington State University https://public.wsu.edu/~pchemlab/documents/Work-functionvalues.pdf(Visited on August 2019)

[32] Fonash S *et al* 2019 *AMPS-1D (BETA version 1.0) Manual* (University Park, PA 16802, Pennsylvania, USA: The Center for Nanotechnology Education and Utilization, The Pennsylvania State University)

[33] Gordon R G 1997 Deposition of transparent conducting oxides for solar cells *AIP Conf. Proc.* **394** 39–48

[34] Gwamuri J, Vora A, Khanal R R, Phillips A B, Heben M J, Guney D O, Bergstrom P, Kulkarni A and Pearce J M 2015 Limitations of ultra-thin transparent conducting oxides for integration into plasmonic-enhanced thin-film solar photovoltaic devices *Mater. Renew. Sustain. Energy* **4** 1–11

[35] Koirala M P and Joshi L P 2017 Structural and optical properties of fluorine doped tin oxide thin film deposited by home built spray pyrolysis unit *Himalayan Phys.* **6–7** 58–60

[36] Green M A, Hishikawa Y, Dunlop E D, Levi D H, Hohl-Ebinger J and Ho-Baillie A W Y 2018 Solar cell efficiency tables (version 52) *Prog. Photovolt. Res. Appl.* **26** 427–36

[37] Impact of series and shunt resistance and temperature, PVeduction.org https://pveducation.org/(Visited on July 2019)